

Data-driven identification of the spatio-temporal structure of turbulent flows by streaming Dynamic Mode Decomposition

Rui Yang^{1,2}, Xuan Zhang¹, Philipp Reiter¹, Moritz Linkmann^{3†},
Detlef Lohse^{1,2} and Olga Shishkina^{1‡}

¹Max Planck Institute for Dynamics and Self-Organisation, Am Fassberg 17, 37077 Göttingen, Germany

²Physics of Fluids Group, Max Planck Center for Complex Fluid Dynamics, MESA+ Institute and J.M.Burgers Center for Fluid Dynamics, University of Twente, P.O. Box 217, 7500 AE Enschede, The Netherlands

³School of Mathematics and Maxwell Institute for Mathematical Sciences, University of Edinburgh, Edinburgh, EH9 3FD, United Kingdom

(Received xx; revised xx; accepted xx)

Streaming Dynamic Mode Decomposition (sDMD) (Hemati *et al.*, Phys. Fluids **26**(2014)) is a low-storage version of Dynamic Mode Decomposition (DMD) (Schmid, J. Fluid Mech. **656** (2010)), a data-driven method to extract spatio-temporal flow patterns. Streaming DMD avoids storing the entire data sequence in memory by approximating the dynamic modes through incremental updates with new available data. In this paper, we use sDMD to identify and extract dominant spatio-temporal structures of different turbulent flows, requiring the analysis of large datasets. First, the efficiency and accuracy of sDMD are compared to the classical DMD, using a publicly available test dataset that consists of velocity field snapshots obtained by direct numerical simulation of a wake flow behind a cylinder. Streaming DMD not only reliably reproduces the most important dynamical features of the flow; our calculations also highlight its advantage in terms of the required computational resources. We subsequently use sDMD to analyse three different turbulent flows that all show some degree of large-scale coherence: rapidly rotating Rayleigh–Bénard convection, horizontal convection and the asymptotic suction boundary layer. Structures of different frequencies and spatial extent can be clearly separated, and the prominent features of the dynamics are captured with just a few dynamic modes. In summary, we demonstrate that sDMD is a powerful tool for the identification of spatio-temporal structures in a wide range of turbulent flows.

1. Introduction

Coherent structures at different spatial and temporal scales are a prominent feature of many turbulent fluid flows occurring in nature and in engineering applications (Yaglom & Tatarski 1967; Holmes *et al.* 1996; Fazole Hussain 1986). Examples include large-scale vortices, wakes, convection rolls and thermal plumes in Rayleigh–Bénard convection (RBC) (Ahlers *et al.* 2009; Lohse & Xia 2010), Taylor rolls in Taylor–Couette flow (Grossmann *et al.* 2016), jets, travelling waves, very-large scale motions (Hutchins & Marusic 2007, 2011) and low-momentum zones (Meinhart & Adrian 1995) that develop in wall-bounded turbulent boundary layers (BLs). These structures are known to have

† Email address for correspondence: Moritz.Linkmann@ed.ac.uk

‡ Email address for correspondence: Olga.Shishkina@ds.mpg.de

manifold significant effects in turbulent flows, for instance influence on heat and mass transport, the occurrence of extreme fluctuations or enhanced drag due their to interaction with near-wall dynamics in turbulent BLs (Monty *et al.* 2007; Marusic *et al.* 2010; Katul 2019). Improving our knowledge of multi-scale spatio-temporal coherence and the underlying physics is of paramount importance as it would lead to a better fundamental understanding of turbulence, specifically in terms of model-building and turbulence control. However, the co-existence of several coherent structures makes the identification and the extraction of particular spatio-temporal features difficult, which led to a growing need for data-driven methods designed to identify and extract patterns.

Modal decomposition, as an umbrella term for a variety of structurally similar methods, identifies structures by decomposing a given dataset in a suitable set of basis functions, or modes. Fourier analysis constitutes perhaps the most well-known and widely used example of a modal decomposition technique. A more sophisticated example is Proper Orthogonal Decomposition (POD) (Berkooz *et al.* 1993; Podvin & Lumley 1998; Rowley *et al.* 2004; Bailon-Cuba *et al.* 2012), where each mode describes a flow structure according to its energy content. However, as the POD modes do not distinguish between different temporal signals, they usually contain more than one characteristic frequency and thus cannot yield information on temporal coherence.

Dynamic Mode Decomposition (DMD), by contrast, decomposes a dataset into spatio-temporal coherent structures (Schmid 2010) with *dynamic modes* obtained as eigenmodes of a high-dimensional linear approximation of the dynamics. More precisely, DMD has solid mathematical foundations in the context of nonlinear dynamical systems theory. Under certain conditions it represents a finite-dimensional approximation to the Koopman operator (Rowley *et al.* 2009; Williams *et al.* 2015), a linear but infinite-dimensional representation of a nonlinear dynamical system (Koopman 1931; Mezić 2005; Mezić 2019). DMD results have an intuitive physical interpretation as each dynamic mode corresponds to a single frequency and growth or decay rate. Therefore, it is a well-suited data-driven method for the analysis of complex datasets and model reduction. Since its introduction by Peter Schmid in 2010 (Schmid 2010), DMD has had a history of successful applications in fluid dynamics such as obtaining low-dimensional dynamic model of the cylinder wake flow (Tissot *et al.* 2014; Bagheri 2013), generating good initial guesses for unstable periodic orbits in turbulent channel flow (Page & Kerswell 2020), flow control (Brunton & Noack 2015; Proctor *et al.* 2016; Rowley & Dawson 2017), aerodynamics (Ghoreyshi *et al.* 2014), and more general in pattern recognition (Jovanović *et al.* 2014; Brunton *et al.* 2016).

Most DMD applications consist of post-processing a time series of experimental or computational data, where most implementations require the access to all data samples at the same instant in time. However, the size of highly resolved turbulent flow data usually precludes saving or loading the entire dataset into memory. Therefore, only a few studies so far have applied DMD to highly turbulent flows. These constraints can be circumvented by a DMD implementation that allows for incremental data updates (Hemati *et al.* 2014; Anantharamu & Mahesh 2019; Zhang *et al.* 2019), such that the DMD calculation proceeds alongside main process such as Direct Numerical Simulations (DNS) or real-time Particle Image Velocimetry (PIV). *Streaming* DMD (sDMD) (Hemati *et al.* 2014) is such a method, which requires only two data samples at a given instant in time and converges to the same results as classical DMD. In what follows we focus on sDMD as a promising method for the analysis of turbulent flows.

The present article is intended to serve two purposes: (a) to demonstrate the applicability of streaming DMD to large datasets of highly turbulent flows relevant to fundamental science and engineering applications, (b) to analyse the spatio-temporal

dynamics of the flow in sub-domains of particular interest. The batch-process streaming version of the DMD algorithm (Hemati *et al.* 2014) is applied to three datasets consisting of time series obtained in DNS of three different turbulent flows: rapidly rotating RBC, horizontal convection (HC) and asymptotic suction boundary layer (ASBL). Despite their physical differences, these three systems share a few features that render them interesting and suitable as test cases to demonstrate the advantages of sDMD for the analysis of turbulent flows.

First, all three cases are paradigmatic examples of fluid-dynamic systems of interest in geophysical fluid dynamics and engineering applications. Rapidly rotating RBC is of relevance whenever rotation and thermal convection are the key physical processes (Ahlers *et al.* 2009; Siggia 1994), such as in the dynamics of planetary cores. Horizontal convection (Hughes & Griffiths 2008; Shishkina *et al.* 2016) occurs in the ocean which is mostly heated and cooled by its upper surface being in contact with the atmosphere. The ASBL (Jones & Watson 1963; Schlichting 1979) is a flat-plate BL with a constant BL thickness in the streamwise direction. The latter is achieved by removing fluid through the pores in the bottom plate. The ASBL therefore allows the application of techniques developed for parallel wall-bounded shear flows to an open flow.

Second, all three systems host spatio-temporally coherent structures. In rapidly rotating RBC, this is the boundary zonal flow, a large-scale travelling wave structure confined to the lateral BLs (Zhang *et al.* 2020; Favier & Knobloch 2020; Shishkina 2020). HC features two characteristic processes that operate on very different time scales, i. e., plume emission and slow oscillatory dynamics in the bulk (Reiter & Shishkina 2020), with the former one being an order of magnitude faster than the latter one. The ASBL shows coherent low momentum zones in the free stream, as do many wall bounded shear flows and freely evolving BLs (Meinhart & Adrian 1995), in the present dataset with a slow spanwise drift.

Third, the size of the datasets presents challenges in all three cases that can be mitigated by the incremental nature of DMD. For rapidly rotating RBC and HC, the fine grids required to properly resolve the small-scale turbulent dynamics result in large datasets, as usual for DNS of turbulent flows. In case of ASBL, a further difficulty lies in the slow dynamics of the low-momentum zone, as an analysis thereof requires very long time series.

This article is organised as follows. Section 2 provides a summary of both, classical DMD (Schmid 2010) and streaming DMD (Hemati *et al.* 2014), where we highlight few subtle differences concerning technical steps and compare our implementations of DMD and sDMD using a standard publicly available dataset – DNS of a developing von-Kármán vortex street. The main results of our analysis concerning turbulent flows are contained in Sec. 3, beginning with rapidly rotating Rayleigh–Bénard convection in Sec. 3.1, followed by horizontal convection in Sec. 3.2 and the asymptotic suction BL in Sec. 3.3. The paper ends with conclusions & an outlook.

2. Dynamic mode decomposition

Before describing the specific features and advantages of streaming DMD (sDMD) (Hemati *et al.* 2014), we briefly summarise the basic ideas and the classical singular value decomposition (SVD) based DMD algorithm (Schmid 2010). For simplicity we restrict ourselves here to the case of equidistant data sequences, for a more general discussion see Kutz *et al.* (2016). Consider a time series of spatially resolved measurement results recorded at a fixed sampling rate $1/\Delta t$ resulting in, say, N equidistant snapshots. Let us further assume that the possibly multidimensional data in each snapshot is

flattened into a corresponding M -dimensional real vector, such that the time series can be represented by an ordered sequence $(\mathbf{x}_k)_{\{k=1,\dots,N\}}$ of column vectors $\mathbf{x}_k \in \mathbb{R}^M$ for $k \in \{1, \dots, N\}$. In the present context \mathbf{x}_k would represent the k^{th} velocity field in a series of N measurements, hence in particular for highly resolved three-dimensional flow fields $M = (\text{number of grid points})^3$ can quickly become very large. We will come back to this point in due course.

The assumption DMD relies upon the existence of a linear operator $\mathbf{A} \in \mathbb{R}^{M \times M}$ which approximates the nonlinear dynamics across the interval Δt , that is

$$\mathbf{x}_{k+1} = \mathbf{A}\mathbf{x}_k + \boldsymbol{\varepsilon}_k \quad \text{for all } k \in \{1, \dots, N-1\}. \quad (2.1)$$

Here, crucially, \mathbf{A} does not depend on k . Finally, $\boldsymbol{\varepsilon}_k$ denotes an error term that is assumed to be small. The validity of this assumption depends on the ratio of the characteristic time scale of the observed nonlinear dynamics and the sampling interval Δt . In practice, \mathbf{A} is chosen by regression over the available data by least-squares minimisation of the $\boldsymbol{\varepsilon}_k$ (Kutz et al. 2016). Since the operator \mathbf{A} describes the spatio-temporal dynamics of the system, its eigenvectors, known as *dynamic modes* or somewhat tautologically DMD modes, may be used to disentangle complex spatio-temporal dynamics and to construct low-dimensional models. In what follows we summarize how the dynamic modes may be determined from the data sequence $(\mathbf{x}_k)_{\{k=1,\dots,N\}}$, following an SVD-based approach as this is what is mostly used in practice owing to numerical stability concerns with the more fundamental Krylov-subspace-type approach and for reasons of computational cost reduction. Further details can be found in the original work by Schmid (2010) and the textbook by Kutz et al. (2016).

2.1. SVD-based DMD

For what follows it is convenient to combine data sequences that consist of $N-1$ samples and are shifted forwards in time by Δt , that is $(\mathbf{x}_k)_{\{k=1,\dots,N-1\}}$ and $(\mathbf{x}_k)_{\{k=2,\dots,N\}}$, into $M \times (N-1)$ -dimensional matrices

$$\mathbf{X} = \mathbf{X}_1^{N-1} = (x_{jk}) := (\mathbf{x}_1 \ \mathbf{x}_2 \ \cdots \ \mathbf{x}_{N-1}) \ , \quad (2.2)$$

$$\mathbf{Y} = \mathbf{X}_2^N = (y_{jk}) := (\mathbf{x}_2 \ \mathbf{x}_3 \ \cdots \ \mathbf{x}_N) \ , \quad (2.3)$$

where $j \in 1, \dots, M$ is the spatial index and k the temporal index. Then Eq. (2.1) implies

$$y_{jk} = x_{jk+1} = \sum_{l=1}^M a_{jl} x_{lk} + \varepsilon_{jk}, \quad \text{or} \quad \mathbf{Y} = \mathbf{A}\mathbf{X} + \mathbf{R} \ , \quad (2.4)$$

where a_{jl} are the entries of the linear operator \mathbf{A} and $\mathbf{R} = (\varepsilon_{jk})$ is the matrix of residuals. The best-fit solution for \mathbf{A} with respect to least-squares minimization of \mathbf{R} is given by $\mathbf{A} = \mathbf{Y}\mathbf{X}^+$, where \mathbf{X}^+ is the pseudo-inverse of \mathbf{X} . In practice, and in particular in fluid dynamics, $M \gg N$ as the dimension M of the spatial samples usually exceeds the number of temporal samples N by far. Hence, $\mathbf{A} \in \mathbb{R}^{M \times M}$ is at most of rank $N-1$, which calls for a lower-dimensional approximation of \mathbf{A} , for instance, by projecting \mathbf{A} on a subspace spanned by, say, r POD modes obtained by calculating the compact SVD of \mathbf{X} ,

$$\mathbf{X} = \mathbf{U}_\mathbf{X} \boldsymbol{\Sigma}_\mathbf{X} \mathbf{W}_\mathbf{X}^T, \quad (2.5)$$

where the superscript T denotes the transpose. The truncation number r is bounded from above by the rank of the data matrix \mathbf{X} , which is at most $N-1$. The columns of $\mathbf{U}_\mathbf{X} \in \mathbb{R}^{M \times r}$ and the rows of $\mathbf{W}_\mathbf{X} \in \mathbb{R}^{r \times M}$ are orthogonal, and $\boldsymbol{\Sigma}_\mathbf{X} \in \mathbb{R}^{r \times r}$ is a diagonal matrix containing the nonzero singular values of \mathbf{X} . The matrix $\mathbf{U}_\mathbf{X}$ contains the spatial

structures of the data sequence, that is, the POD modes are given by the columns of $\mathbf{U}_\mathbf{X}$. By substitution of Eq. (2.5) into Eq. (2.4) and subsequent rearrangement, one obtains

$$\mathbf{S} := \mathbf{U}_\mathbf{X}^T \mathbf{A} \mathbf{U}_\mathbf{X} \approx \mathbf{U}_\mathbf{X}^T \mathbf{Y} \mathbf{W}_\mathbf{X} \mathbf{\Sigma}_\mathbf{X}^{-1} \in \mathbb{R}^{r \times r}. \quad (2.6)$$

This equation is to be interpreted in a least-squares optimal sense (hence the absence of the residual), as it can also be obtained by calculating \mathbf{A} through the pseudo-inverse of \mathbf{X} , which is calculated via SVD, and subsequently projecting \mathbf{A} onto the $r_\mathbf{A}$ -dimensional subspace spanned by the POD modes. Since \mathbf{A} and \mathbf{S} are related by a similarity transform, the eigenvalues of \mathbf{S} correspond to the non-zero eigenvalues of \mathbf{A} . For practical purposes we summarize the SVD-based DMD algorithm (Schmid 2010) as follows:

- Collect N temporally equidistant samples $\{\mathbf{x}_1, \mathbf{x}_2, \mathbf{x}_3, \dots, \mathbf{x}_N\}, \mathbf{x}_j \in \mathbb{R}^M, j \in \{1, \dots, N\}$.
- Build a matrix $\mathbf{X} \in \mathbb{R}^{M \times (N-1)}$ out of the first $(N-1)$ snapshots, according to Eq. (2.2).
- Calculate the compact SVD of \mathbf{X} according to Eq. (2.5).
- Build a matrix $\mathbf{Y} \in \mathbb{R}^{M \times (N-1)}$ out of the last $(N-1)$ snapshots, according to Eq. (2.3) and combine it with the matrices $\mathbf{U}_\mathbf{X}$ and $\mathbf{W}_\mathbf{X}$ to calculate the optimal representation \mathbf{S} of the linear mapping \mathbf{A} in the orthogonal basis given by the POD modes according to Eq. (2.6).
- Calculate the eigenvectors \mathbf{v}_k and eigenvalues λ_k of \mathbf{S} for $k \in \{1, \dots, r\}$.
- Calculate the (projected) dynamic modes ψ_k

$$\psi_k = \mathbf{U} \mathbf{v}_k. \quad (2.7)$$

The data vector \mathbf{x} , or, in the present context the velocity field, at time t can then be approximated using $N' \leq r$ dynamic modes and their corresponding DMD eigenvalues

$$\mathbf{x}(t) \approx \sum_{k=1}^{N'} a_k e^{(\sigma_k + i\omega_k)t} \psi_k, \quad (2.8)$$

where a_k are the diagonal elements of $\mathbf{\Sigma} = \text{diag}(a_1, \dots, a_r)$, representing the amplitude for each mode, and

$$\omega_k = \frac{\text{Im}(\ln(\lambda_k))}{\Delta t}, \quad \sigma_k = \frac{\text{Re}(\ln(\lambda_k))}{\Delta t}. \quad (2.9)$$

are the frequency and temporal growth or decay rate of the k^{th} dynamic mode for $k \in \{1, \dots, r\}$, respectively. The accuracy of the approximation does not only depend on the number of dynamic modes used to reconstruct the data, it also depends on truncation number r , which determines the accuracy with which the projected dynamic modes have been calculated. Several truncation criteria have been developed to determine a suitable value for r , such as sparsity-promoting algorithm (Jovanović *et al.* 2014), Optimal Singular Value Hard Threshold (Gavish & Donoho 2014) and improved rank based on space sampling (Kou & Zhang 2017).

2.2. Streaming DMD

Classical DMD requires access to the entire data sequence at once, which precludes the analysis of large datasets due to memory constraints. This applies to data of either a high degree of spatial or temporal complexity, where the former results in high spatial dimensionality (large M) and the latter requires long time series (large N) to capture the temporal features of the dynamics. Streaming DMD is a method for the calculation of the POD-projected linear operator \mathbf{S} based on incremental data updates that addresses

this challenge by only requiring two data samples to be held in memory at a given time (Hemati et al. 2014). In what follows we summarize this procedure; further details including processing steps that reduce the effects of data contamination by noise can be found in the original work by Hemati et al. (2014). Streaming DMD consists of two conceptual parts, a low-storage calculation of \mathbf{S} , and a scheme to update \mathbf{S} using new data samples based on the iterative Gram–Schmidt orthogonalization.

Let us re-consider the data matrices \mathbf{X} and \mathbf{Y} defined in Eqs. (2.2) and (2.3) and write Eq. (2.6) as

$$\mathbf{S} = \mathbf{U}_{\mathbf{X}}^T \mathbf{Y} (\mathbf{U}_{\mathbf{X}}^T \mathbf{X})^+ = \mathbf{U}_{\mathbf{X}}^T \mathbf{U}_{\mathbf{Y}} \tilde{\mathbf{Y}} \tilde{\mathbf{X}}^+ = \mathbf{U}_{\mathbf{X}}^T \mathbf{U}_{\mathbf{Y}} \tilde{\mathbf{Y}} \tilde{\mathbf{X}}^T (\tilde{\mathbf{X}} \tilde{\mathbf{X}}^T)^+ = \mathbf{U}_{\mathbf{X}}^T \mathbf{U}_{\mathbf{Y}} \mathbf{H} \mathbf{G}_{\mathbf{X}}^+, \quad (2.10)$$

where $\tilde{\mathbf{Y}} := \mathbf{U}_{\mathbf{Y}}^T \mathbf{Y} \in \mathbb{R}^{r_{\mathbf{Y}} \times N-1}$ and $\tilde{\mathbf{X}} := \mathbf{U}_{\mathbf{X}}^T \mathbf{X} \in \mathbb{R}^{r_{\mathbf{X}} \times N-1}$ and the identity $\tilde{\mathbf{X}}^+ = \tilde{\mathbf{X}}^T (\tilde{\mathbf{X}} \tilde{\mathbf{X}}^T)^+$, which can be readily verified via SVD, was used in the penultimate step. That is, now both data matrices \mathbf{X} and \mathbf{Y} are projected onto orthogonal bases consisting of their respective left singular vectors, the POD-modes, with truncation numbers $r_{\mathbf{X}} \leq \text{rank } \mathbf{X}$ and $r_{\mathbf{Y}} \leq \text{rank } \mathbf{Y}$. The rearrangement carried out in the penultimate step has the advantage that $\mathbf{H} := \tilde{\mathbf{Y}} \tilde{\mathbf{X}}^T \in \mathbb{R}^{r_{\mathbf{Y}} \times r_{\mathbf{X}}}$ and $\mathbf{G}_{\mathbf{X}} = \tilde{\mathbf{X}} \tilde{\mathbf{X}}^T \in \mathbb{R}^{r_{\mathbf{X}} \times r_{\mathbf{X}}}$, which in itself is an improvement of the classical DMD in terms of memory usage as long as $r_{\mathbf{X}} < M$ and $r_{\mathbf{Y}} < M$. Especially in fluid dynamics, this is often the case unless the data is very noisy. We will come back to this issue in due course. However, the main advantage of the formulation in Eq. (2.10) lies in the fact that all matrices on the right-hand side of Eq. (2.10) can be obtained incrementally from a data stream using only two samples at a time. The matrices $\mathbf{U}_{\mathbf{X}}$ and $\mathbf{U}_{\mathbf{Y}}$ can be calculated incrementally from the data stream by iterative Gram-Schmidt orthogonalization. After each orthogonalization step the updated orthogonal matrices are then used to project the sample vectors onto the respective bases, and the matrices \mathbf{H} and $\mathbf{G}_{\mathbf{X}}$ are subsequently constructed from the projected sample vectors. More precisely, consider for instance the k^{th} pair of sample vectors \mathbf{x}_k and $\mathbf{y}_k = \mathbf{x}_{k+1}$. The matrices $\mathbf{U}_{\mathbf{X}}$ and $\mathbf{U}_{\mathbf{Y}}$, which have been constructed incrementally from the previous data samples, are now updated using \mathbf{x}_k and the newly available \mathbf{y}_k . Then, $\tilde{\mathbf{x}}_k = \mathbf{U}_{\mathbf{X}}^T \mathbf{x}_k$ and $\tilde{\mathbf{y}}_k = \mathbf{U}_{\mathbf{Y}}^T \mathbf{y}_k$ are calculated and we can update the remaining matrices according to

$$\mathbf{H} = \sum_{l=1}^k \tilde{\mathbf{y}}_l \tilde{\mathbf{x}}_l^T \quad \text{and} \quad \mathbf{G}_{\mathbf{X}} = \sum_{l=1}^k \tilde{\mathbf{x}}_l \tilde{\mathbf{x}}_l^T. \quad (2.11)$$

Before proceeding to the calculations, a few comments are in order. First, the incremental nature of the method precludes the application of numerically more stable orthogonalization methods such as Householder reflections, and this may affect the convergence properties of the method. Second, experimental noise may result in a drastic decrease in computational efficiency as noise usually results in the data matrices being of high rank. In practice, this can be mitigated through an intermediate processing step, as explained in detail in Hemati et al. (2014). Third, we note that $\mathbf{G}_{\mathbf{X}} = \boldsymbol{\Sigma}_{\mathbf{X}} \boldsymbol{\Sigma}_{\mathbf{X}}$ contains the squares of the nonzero singular values of \mathbf{X} , as can be verified via SVD.

2.3. Validation

Before applying sDMD to the three aforementioned datasets, we first validate and compare the classical and streaming DMD implementation using the publicly available dataset provided by Kutz et al. (2016). Subsequently, we use this dataset to test a coarsening interpolation scheme designed to reduce the computational effort when analysing data of high spatial dimension M , as is the case for turbulence. Since the focus of the

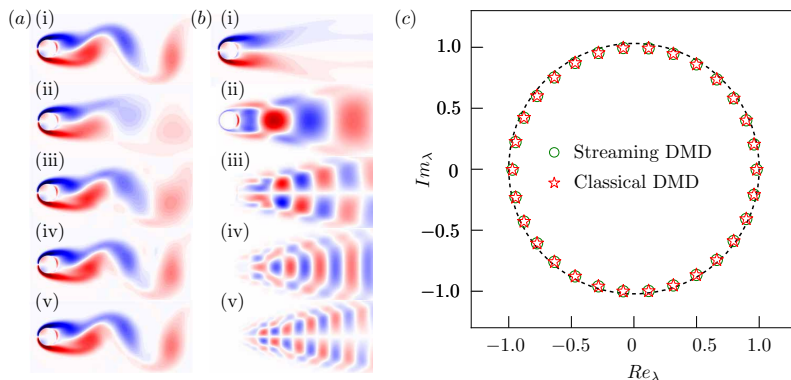


FIGURE 1. Streaming DMD results for two-dimensional vortex shedding behind a cylinder at $Re = 100$ using in total 150 vorticity-field samples and a truncation mode number of $r = 30$. (a) Original and reconstructed vorticity fields. Cyclonic vortices are shown in blue and anticyclonic vortices in red. Panel (i) presents the original field and (ii)-(v) the reconstructed fields using two to five dynamic modes. (b) The first five dynamic modes used in the reconstructions. (c) Comparison of DMD eigenvalues obtained from SVD-based DMD (Schmid 2010) and streaming DMD (Hemati *et al.* 2014).

present work lies in the identification of the most dominant structures of the system, usually represented by one or two the most important modes, we do not apply any specific algorithm to determine the truncation number r . Instead, different values of r were tested to ensure convergence, resulting in $r = 30$ as a sufficient truncation number.

2.3.1. Comparison between sDMD and DMD

The dataset provided in Kutz *et al.* (2016) consists of a time series of two-dimensional vorticity fields obtained by computer simulation of the wake flow behind a cylinder for Reynolds number $Re = UD/\nu = 100$, where U , D and ν denote the free-stream velocity, the diameter of the cylinder and the kinematic viscosity of the fluid. The dominant dynamics are governed by periodic vortex shedding, and therefore very well suited for DMD validation. For details on the numerical method used to generate the data we refer to the original reference (Kutz *et al.* 2016). In total, 151 vorticity-field samples, separated by a time interval $\Delta t = 0.2$, were analysed. A typical sample is shown in figure 1a(i), where the flow evolves from left to right shedding cyclonic vortices in blue (dark grey) and anticyclonic vortices in red (light grey) at a Re -dependent frequency f . The vortex-shedding frequency can be expressed in non-dimensional form through the Strouhal number $St = fD/U$. For the present dataset at $Re = 100$, the Strouhal number is around $St = 0.16$.

Figures 1a(ii)-(v) present reconstructions of the vorticity field with an increasing number of dynamic modes (2-5) calculated via sDMD using a projection onto 30 POD modes. The first mode shown in figure 1b(i) has an eigenvalue of 1 and represents the mean vorticity field. The second dominant DMD eigenmode shown in figure 1b(ii) corresponds to the vortex shedding frequency. The frequency of the second mode is given by $Im(\log(\lambda_2)/(2\pi\Delta t))$, where λ_2 is the corresponding eigenvalue. We obtain $\lambda_2 = 0.9875 - 0.2063i$, resulting in a dimensionless frequency, or Strouhal number of $St = 0.165$, which is in good agreement of the expected Strouhal number at $Re = 100$. The following modes visualised in figures 1b(iii,iv,v) show higher-order coherent structures in the vorticity field. As can be seen from the visualisations of the reconstructed vorticity field in figures 1a(i) and (ii), and from the measured frequency of the second dynamic

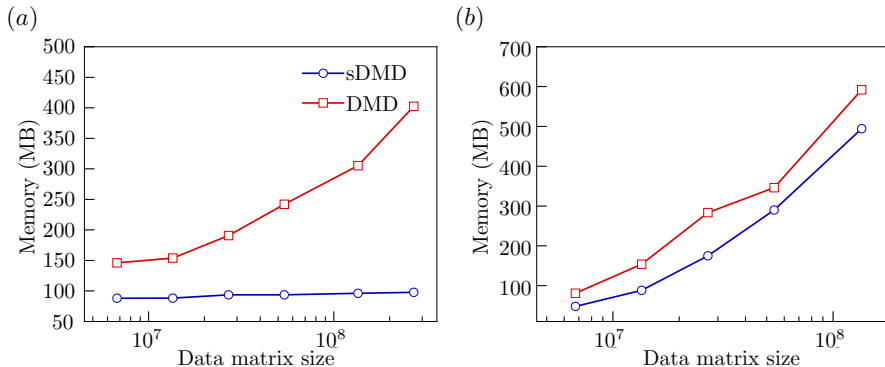


FIGURE 2. Memory consumption of the classical SVD-based DMD method and streaming DMD method as a function of the data matrix size given by the sample size times the number of samples in the time series. (a) Fixed sample size and varying number of samples in the time series. (b) Fixed number of samples with varying sample size.

mode, vortex shedding is well described by the first two modes. With only four modes, the reconstructed vorticity field (figure 1a(v)) is already visually indistinguishable from the original shown in figure 1a(i). This demonstrates the efficiency of the DMD for periodic flows.

The same calculations were carried out using the classical DMD algorithm. In figure 1c we compare the spectra of the linear operator \mathbf{S} obtained from standard DMD and streaming DMD. As the dynamics are nonlinear and statistically stationary, for sufficiently long time series all transiently growing processes will undergo nonlinear saturation while the amplitude of decaying process will essentially vanish and the eigenvalues are expected to be neutrally stable (Horn & Schmid 2017), i.e. lie on the unit circle. This is indeed the case. Furthermore, the eigenvalues obtained with the two methods coincide.

The memory consumption of both methods as a function of the data matrix size, defined as the product of the sample size times the number of samples in the time series, is presented in figures 2(a,b). In order to ensure consistency, all tests were carried out on the same computer with an Intel i5-8250U CPU at 1.60GHz and 8GB RAM. In figure 2(a), the individual sample size was held fixed such that an increase in the data matrix size is achieved through a larger number of samples in the time series. As expected, the memory consumption of classical DMD grows with increasing data matrix size while the memory consumption of sDMD remains almost constant. In contrast, in figure 2(b), the number of samples in the time series is constant and the data matrix size increases with sample size. In this case, the increase in memory consumption is qualitatively similar between the two methods, albeit at an offset in favour of sDMD.

2.3.2. Coarse interpolation for the analysis of high-dimensional data

Numerical simulations of highly turbulent flows require fine computational grids to accurately resolve the dynamics at the small scales. This is not necessarily always due to a need to precisely measure small-scale quantities such as dissipation, but also concerns numerical stability. The required large number of grid points results in a high memory load even for a single sample, which quickly becomes prohibitive even for sDMD. This calls for a reliable downsampling strategy to interpolate the data on coarser grids. In what follows we analyse the robustness of sDMD with respect to different degrees of spatial downsampling, using the same vortex shedding dataset of the previous subsection. The downsampling was carried out by successively decreasing the original number of grid

points, beginning with 90000 grid points down to a minimum of 5 grid points. The effect of downsampling is assessed by considering two observables, the DMD eigenvalues and the time-averaged reconstruction error, defined as

$$\varepsilon_2 := \langle \|\mathbf{v}(t_0) - \sum_{k=1}^{N'} a_k e^{(\sigma_k + i\omega_k)t_0} \psi_k\|_2 \rangle_t, \quad (2.12)$$

where \mathbf{v} denotes the vorticity field here, and the angled brackets denote a time average. The results are summarized in figure 3, with figure 3(a) and (b) showing the streaming DMD eigenvalues for the original data and after different degrees of downsampling, Figure 3(c) the reconstruction error as a function of the data matrix size for classical DMD and sDMD, and figure 3(d) presenting visualisations of a sample of the reconstructed vorticity fields after different degrees of downsampling. A number of observations can be made from figure 3. The DMD eigenvalues are remarkably robust under the downsampling procedure. As can be seen from the data shown in figures 3(a) and (b), a reduction by three orders of magnitude in the data matrix size results in almost the same values for the DMD eigenvalues. Significant qualitative differences in the eigenvalues occur only after drastic downsampling from 90000 to less than 10 data points. A more quantitative comparison is achieved by considering the difference ε_1 between the Strouhal number and the dimensionless frequency of the second dynamic mode as a function of the data matrix size presented in figure 3(c). As can be seen from the figure, the Strouhal number is reproduced very accurately using only 25 data points. This is particularly striking in view of the unsurprisingly large reconstruction error ε of order 10^{-3} to 10^{-2} , for the corresponding downsampled data, as shown in figure 3(d). According to the data presented in the figure, converged results for the reconstruction of the full vorticity field requires at data matrix size of least 9000 points. The finite residual for higher resolved data is then due to truncation in the DMD algorithm. The visualisations of the reconstructed vorticity fields in figure 3(e) give a visual impression of the effect the downsampling has on the reconstructed data. As expected, the large-scale spatial coherence is still present in the downsampled data. Since the focus is on the detection of large-scale coherent structures, like the vortex street in this case, and since the coarsening interpolation results in the removal of small-scale spatial structures, the downsampling has very little effect on the results, as expected.

3. Results

Having validated our implementation of sDMD on publicly available data, we now apply the method to three different flows, rapidly rotating Rayleigh–Bénard convection (RBC), horizontal convection (HC), and the asymptotic suction boundary layer (ASBL). We chose these three examples in order to demonstrate sDMD to be a useful tool for the analysis of different turbulent flows in terms of their main spatio-temporal structure.

In rapidly rotating RBC, the anticyclonic circulation in the bulk is surrounded by a cyclonic layer close to the horizontal cell walls, and the aim is to identify this large-scale flow pattern. Horizontal convection lends itself well as a test case for the distinction of different spatio-temporal structures, as the dynamics is largely governed by two instabilities that operate on different time scales. The Rayleigh–Taylor instability leads to fast periodic plume generation close to the boundary while an oscillatory instability in the bulk results in much slower periodic dynamics in the bulk. The respective frequencies associated with these two processes differ by an order of magnitude. Similar to canonical wall-bounded parallel shear flows and spatially developing BLs, the ASBL features long-

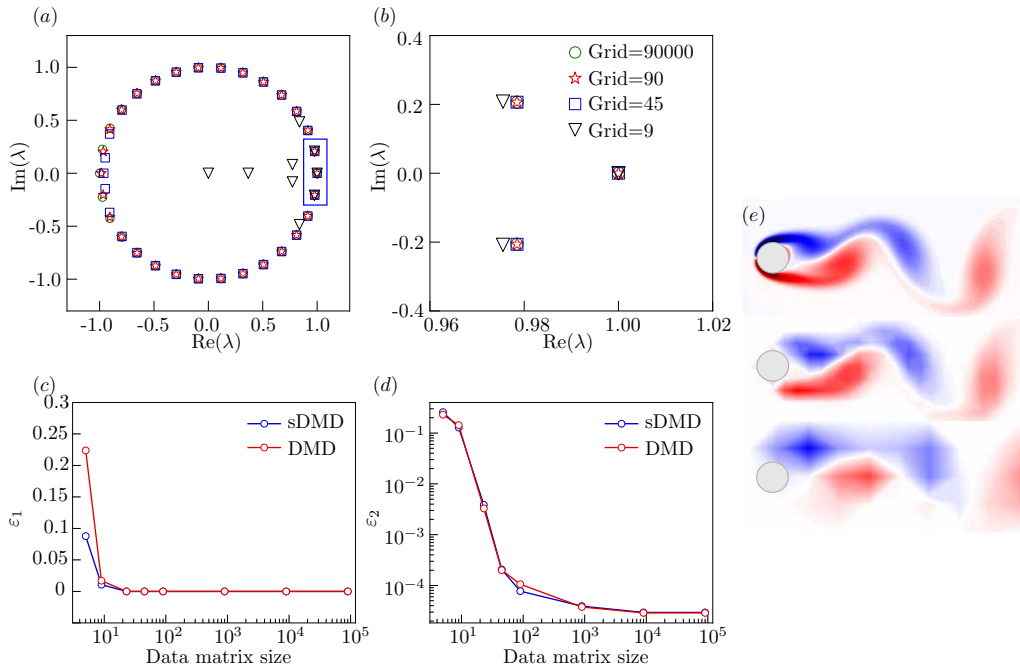


FIGURE 3. (a) Streaming DMD eigenvalues for the original data (green circles) and after different degrees of downsampling. (b) Magnification of the blue region in (a). (c) Error of the Strouhal number as a function of the downsampled data matrix size for classical DMD and sDMD. (d) The time-averaged reconstruction error as defined in Eq. (2.12) as a function of the downsampled data matrix size for classical DMD and sDMD. (e) The instantaneous flow field on 90000, 900 and 100 grid points, respectively, from top to bottom.

lived large-scale coherent motion. Here the aim is to identify the corresponding spatio-temporal structure. The slow dynamics requires very long time series, which makes this example particularly suitable for the application of sDMD.

All datasets were obtained by direct numerical simulation at parameter values corresponding to turbulent flow. Further details on the numerical methods and parameter values will be given in the following subsections.

3.1. Rapidly Rotating Rayleigh–Bénard Convection

3.1.1. Fluid flow

In rotating Rayleigh–Bénard convection, a fluid is confined between a heated bottom plate and a cooled top plate and is rotated around a vertical axis. It is a paradigmatic problem to study many geophysical and astrophysical phenomena in the laboratory, e.g. convective motion occurring in the oceans, the atmosphere, in the outer layer of stars, or in the metallic core of planets. In rotating RBC laboratory experiment, the fluid is laterally confined. The centrifugal force can be neglected, provided the Froude number is small, and then only the Coriolis force is considered. The interplay of the occurring buoyancy and Coriolis forces, however, may yield highly complex flows with very distinct flow structures whose nature strongly depends on the control parameters. Without rotation or with slow rotation, a distinct feature of turbulent RBC is the emergence of the Large-Scale Circulation (LSC) of fluid. For rapid rotation, however, a cyclonic azimuthal velocity boundary-layer flow, the Boundary Zonal Flow (BZF),

develops close to the side walls, surrounding a core region of anticyclonic circulation. The viscous Ekman BLs near the plates induce an anticyclonic circulation with radial outflow in horizontal planes, which is balanced by the vertical velocity in a thin annular region near the sidewall, where cyclonic vorticity is concentrated. The Taylor–Proudman effect induced by rapid rotation tends to homogenize the flow in the vertical direction. The temperature pattern near the vertical wall, however, moves anticyclonically within the BZF and is connected to the thin anticyclonic Ekman layers at the top and bottom plates. The aim here is to recover the BZF via sDMD.

3.1.2. Dynamic equations & control parameters

We consider RBC in a vertical cylinder rotating with uniform angular velocity Ω about the vertical axis. The governing equations of the problem are the incompressible Navier–Stokes equations in the Oberbeck–Boussinesq approximation, coupled with the temperature equation, given here in dimensionless form

$$\partial_t \mathbf{u} + (\mathbf{u} \cdot \nabla) \mathbf{u} + \nabla p = \sqrt{Pr/Ra} \nabla^2 \mathbf{u} - Ro^{-1} \hat{z} \times \mathbf{u} + T \hat{z}, \quad (3.1)$$

$$\partial_t T + (\mathbf{u} \cdot \nabla) T = \sqrt{1/(PrRa)} \nabla^2 T, \quad (3.2)$$

$$\nabla \cdot \mathbf{u} = 0. \quad (3.3)$$

The Rayleigh number, Ra , describes the strength of the thermal buoyancy force, the Prandtl number, Pr , the ratio of viscosity and diffusivity, and the convective Rossby number, Ro , is a measure for the rotation rate. They are defined as

$$Ra \equiv \alpha g \Delta H^3 / \kappa \nu, \quad Pr \equiv \nu / \kappa, \quad Ro \equiv \sqrt{\alpha g \Delta H} / 2 \Omega H, \quad (3.4)$$

where α denotes the isobaric expansion coefficient, g the acceleration due to gravity, H the fluid layer height, $\Delta = T_+ - T_-$ the imposed adverse temperature difference with T_+ (T_-) being the temperature of the heated bottom (cooled top) plate, κ the thermal diffusivity, ν the kinematic viscosity, and Ω the angular rotation speed. Equations (3.1)–(3.3) were stepped forward in time using the finite-volume code GOLGFISH (Shishkina *et al.* 2015; Kooij *et al.* 2018; Zhang *et al.* 2020). For the temperature we impose Dirichlet boundary conditions (isothermal) on the top and bottom plates and Neumann conditions (adiabatic) on the lateral walls. All boundaries are assumed to be impenetrable and no-slip, i. e. the velocity field vanishes at all boundaries.

3.1.3. Numerical details

We consider datasets for two different Rayleigh numbers, $Ra = 10^8$ and $Ra = 10^9$, the remaining control parameters are $Pr = 0.8$, $Ro = 0.1$. The resolution of the original datasets is $N_r \times N_\phi \times N_z = 322 \times 82 \times 256$ for $Ra = 10^8$ and $N_r \times N_\phi \times N_z = 822 \times 194 \times 512$ for $Ra = 10^9$, according to Shishkina *et al.* (2010), where N_r , N_ϕ and N_z denote the number of grid points in radial, azimuthal and vertical direction, respectively. The velocity fields from both datasets are sampled for a time period of 400 free-fall time units with a sampling interval of $\Delta t = 2.5$, resulting in 160 samples in total. Both datasets are spatially downsampled for the sDMD analysis, by a four-fold and a 16-fold reduction in the number of data points, respectively, resulting in a spatial resolution of $N_r \times N_\phi \times N_z = 161 \times 82 \times 128$ for $Ra = 10^8$ and $N_r \times N_\phi \times N_z = 256 \times 96 \times 128$ for $Ra = 10^9$. The truncation number is $r = 40$ in both cases. In what follows we first describe the generic spatial features that can be extracted with the first few dynamic mode for the case $Ra = 10^8$ and subsequently consider the temporal features for both $Ra = 10^8$ and $Ra = 10^9$.

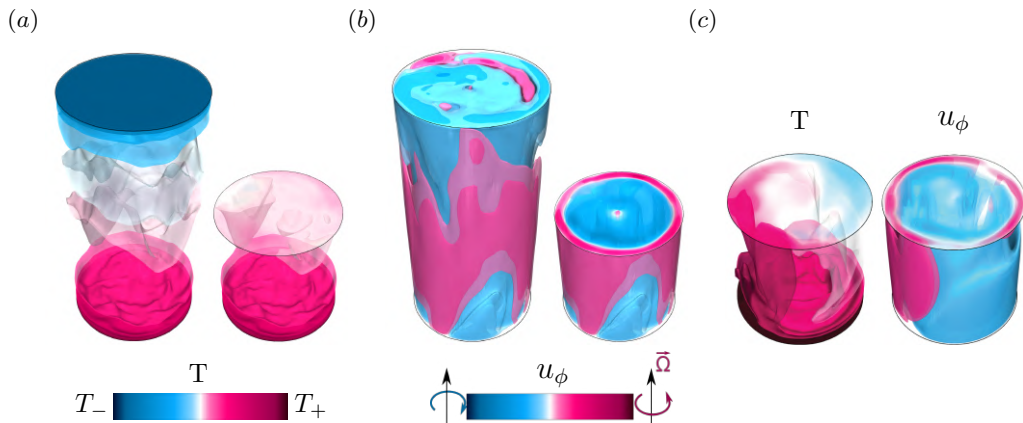


FIGURE 4. The first two dynamic modes for $Pr = 0.8$, $Ra = 10^8$ and $Ro = 0.1$. (a) The first mode of the anticyclonic drifting temperature field in the full cell (left) and in the bottom half of the cell (right). (b) The first mode of the azimuthal velocity field in the full cell (left) and in the bottom half of the cell (right). (c) The second mode of the temperature (left) and the azimuthal velocity field (right) in the bottom half of the cell.

3.1.4. Streaming DMD

The first two dynamic modes obtained from the $Ra = 10^8$ -dataset are visualised in figure 4 in terms of temperature and azimuthal velocity. The temperature field of the first dynamic mode shown in figure 4(a) resembles the mean temperature profile, the corresponding azimuthal velocity field (figure 4 b) consists of anticyclonic motion in the bulk and cyclonic motion close to the sidewall. As expected, the first dominant mode corresponds to a base or mean flow. However, this mode is evidently dynamically not important without temporal change. The principal mode is the second one, presented in figure 4(c), and the BZF (Zhang *et al.* 2020) is clearly visible, both in the temperature (left) and azimuthal velocity (right).

Even though the flow is turbulent, its large-scale spatial structure can be reconstructed nicely with only a few modes as demonstrated by the visualisation of the azimuthal velocity in the lower half of the RBC-cell presented in figure 5. We point out that much of the small-scale dynamics and thereby accuracy in the representation is lost through the downsampling procedure, and applying streaming DMD without coarse interpolation but with larger memory consumption may be advisable if the focus is on a more detailed reconstruction of the flow. Here, we focus only on the large-scale structure. The comparison is carried out for two velocity fields which have been sampled about 30 free-fall times apart in order to guarantee sufficiently decorrelated samples. The originals are shown in figures 5(a) and (d), respectively. Figures 5(b) and (e) contain the reconstructions using the first two modes, and figures 5(c) and (f) the reconstructions from the first five modes for the two samples, respectively. These examples demonstrate consistently that even though the main features of the flow can be captured by the mean flow and the BZF, a fair amount of detail is missing and its inclusion requires a few more modes. A much better reconstruction can be achieved with as little as five modes.

Having discussed the identification of the dominant spatial feature of the flow, the BZF, we now focus on its temporal structure. Figure 6 presents spatio-temporally resolved diagrams of the dynamics in a ring located at half-height $z = H/2$ and at radial location $r = r_{u_\phi}^{\max}$, where the maximum azimuthal velocity is observed, as indicated

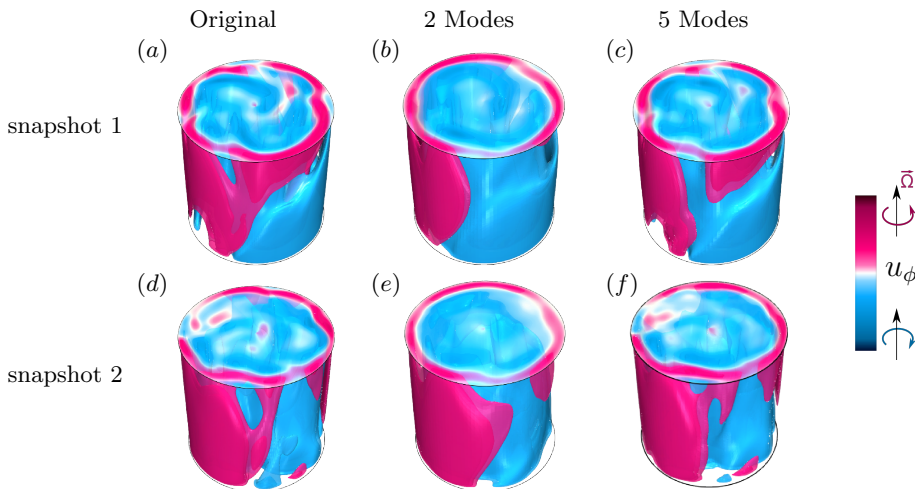


FIGURE 5. Reconstructed azimuthal velocity field for two different velocity-field samples for $Pr = 0.8$, $Ra = 10^8$ and $Ro = 0.1$. (a), (d) original field, (b), (e) reconstruction with two dynamic modes, (c), (f) reconstruction with five dynamic modes.

by the red circle in the schematic drawing shown in figure 6(a). The time evolution of the temperature and vertical velocity fields of the $Ra = 10^8$ -dataset are presented in figure 6(b) and (c), respectively, while figure 6(d) corresponds to the time-evolution of the temperature field at $Ra = 10^9$. The original data is shown in the left panels of the respective visualisations and the data reconstructed from the first two dynamic modes is shown in the right panels. Visual comparison of the left and right panels confirms again the the zonal flow pattern can be clearly captured with only the first two dynamic modes, the mean flow and the BZF. Furthermore, the visualisations clearly identify the BZF as a travelling wave with strongly correlated temperature and vertical velocity fields as can be seen by comparison of figure 6(b) and (c). The travelling wave structure of the BZF is also present at higher Ra , as can be seen in figure 6(d). As such, it seems to be a robust feature of the BZF in the Rayleigh-number range considered here. However, according to the visualisation the dynamics appear to be slightly more complex at $Ra = 10^9$ than at $Ra = 10^8$, hence it remains to be seen to what extent the travelling wave dynamics persist with increasing Ra .

In summary, the most prominent spatio-temporal features of rapidly rotating RBC can be identified through sDMD, with the BZF emerging as the dominant dynamic mode. The cyclonic motion of the fluid reflected in the azimuthal velocity and the anticyclonic motion of the flow pattern reflected in the temperature and vertical velocity as well as their frequencies are fully reproduced by only the first two dynamic modes. These results firmly establish sDMD as a powerful tool for the extraction of dominant coherent structures in turbulent rapidly rotating RBC.

3.2. Horizontal Convection

3.2.1. Fluid flow

Horizontal convection (HC), similarly to RBC, is driven by thermal buoyancy. However, in HC heating and cooling are applied to different parts of the same horizontal surface. In our case, the heated plate is located in the center and the cooled plates are placed at both ends, as shown in figure 7(a). This setup is relevant for many geophysical

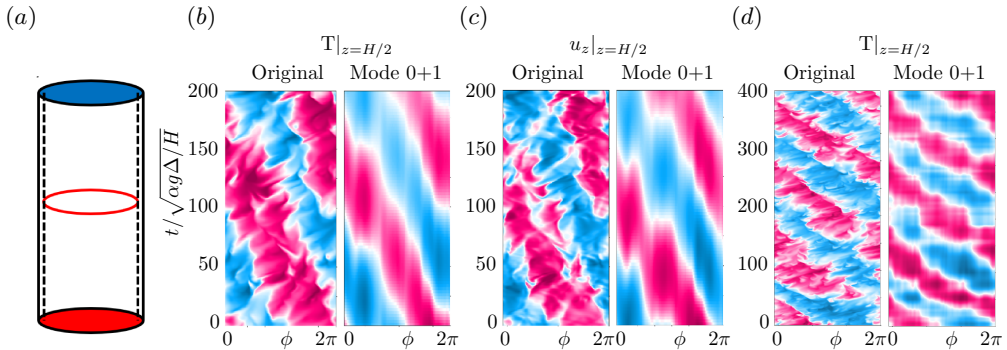


FIGURE 6. Time evolution of temperature and vertical velocity. (a) Schematic setup. The red circle indicates the location where temperature and velocity were measured. (b) temperature field and (c) vertical velocity field for $Ra = 10^8$, and (d) temperature field for $Ra = 10^9$. The original fields are shown in the left panels and the right panels correspond to the reconstructed field using two dynamic modes. The color scale varies from minimum values indicated in blue to maximum values indicated in magenta for the respective fields, given by temperatures at the top and bottom plates in (b) and (d), and $[-u_{ff}/2, u_{ff}/2]$ with $u_{ff} \equiv \sqrt{\alpha\Delta gR}$ being the free-fall velocity in (c).

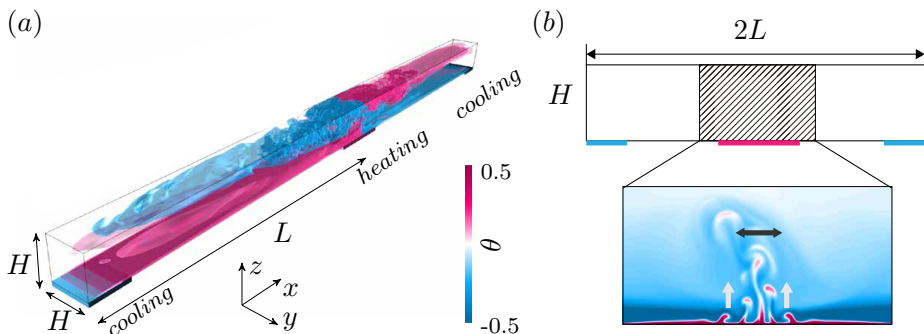


FIGURE 7. Sketch of (a) HC adapted from [Reiter & Shishkina \(2020\)](#) and (b) front view of the setup. Only the shaded area (b) is used for sDMD. The inset shows a snapshot of the temperature field for $Ra = 10^{11}$ and $Pr = 10$. There, the grey arrows indicate the motion of the periodically detaching plumes; the dark arrow indicates the oscillatory motion inside the bulk region.

and astrophysical flows ([Scott *et al.* 2001](#); [Spiegel 1971](#)) and engineering applications ([Gramberg *et al.* 2007](#)), in particular concerning the large-scale overturning circulation of the ocean as heat is supplied to and removed from the ocean predominantly through its upper surface, where the ocean contacts the atmosphere. The dimensionless control parameters are similar to RBC, that is the Rayleigh number, the Prandtl number and the aspect ratio Γ ,

$$Ra \equiv \alpha g \Delta L^3 / (\kappa \nu), \quad Pr \equiv \nu / \kappa, \quad \Gamma \equiv L / H = 10,$$

where the characteristic length scale L is the half-cell length. The governing equations are again the incompressible Navier–Stokes equations in the Oberbeck–Boussinesq approximation, and a temperature equation stated in Eqs. (3.1)–(3.3), but without the Coriolis term in the momentum equation.

For the parameters $Ra = 10^{11}$ and $Pr = 10$ it was observed that sheared plumes,

originated by a Rayleigh–Taylor instability, periodically arise above the heated plate and travel towards the center (Reiter & Shishkina 2020). However, another time-dependent feature that emerges is the oscillatory instability that breaks symmetry inside the bulk region, see figure 7 (b). So there is a fast periodic emission of thermal plumes close to the boundary and a slow periodic oscillation in the bulk region. Streaming DMD is used to separate these two coexisting dynamics.

3.2.2. Dynamic equations & numerical details

The dataset consists of velocity fields obtained in the DNS for a rectangular geometry, as shown in the schematic drawing in figure 7(a). The temperature boundary conditions at the bottom plate are $\theta = 0.5$ for $0 \leq x \leq 0.1$ and $\theta = -0.5$ for $0.9 \leq x \leq 1$, all the other walls are adiabatic. No-slip boundary conditions are imposed at all walls for the velocity field. The calculations were carried out using the GOLDFISH code, as in the previous section. Further details can be found in Reiter & Shishkina (2020). The original grid is $N_x \times N_y \times N_z = 66 \times 1026 \times 98$, where N_x , N_y , and N_z , denote the number of grid points in the mean-flow x -direction, the spanwise y -direction and the z -direction, which is normal to the heated and cooled bottom plates, respectively. Though, since plumes and oscillations are concentrated above the heated plate, we extract only the data inside the shaded domain, shown in figure 7(b), with $N_x \times N_y \times N_z = 66 \times 200 \times 98$. The truncation number r is set to 80 to ensure the dominant modes can be captured properly. Since the plume emission motion is more than ten times faster than the oscillatory flow, a small time interval is needed to capture the fast plume emission while a large number of velocity-field samples is required to simultaneously identify the slow oscillations. To save computational resources, we decouple the two tasks and use two datasets comprised of 200 snapshots each, sampled at different time intervals: 0.1 free-fall time units for the fast plume emission and 0.5 free-fall time units for the slow oscillatory flow.

3.2.3. Streaming DMD

The temporal structure of the original temperature field and the temperature field reconstructed from the first two dynamic modes is shown in figure 8 using horizontal slices located at the spanwise middle of the domain, $y = H/2$, and at different heights. Figures 8(a) and (b) contain visualisations of the original field at $z = 0.1H$, to capture fast plume emission, and at $z = 0.8H$, to capture slow oscillations, respectively, and figures 8(c) and (d) present the corresponding reconstructions. A visual comparison of the original and the reconstructed fields qualitatively shows that sDMD can clearly distinguish the two dominant spatio-temporal structures, with the first two dynamic modes identifying the fast motion of the plume emission for the dataset sampled at 0.1 free-fall time units (figures 8(a) and (c)), and the first two dynamic modes capturing the slow oscillatory mode for the dataset sampled at 0.5 free-fall time units (figures 8(b) and (d)). The frequencies obtained from the DNS data and the sDMD calculations are compared with the DMD frequencies being calculated according to Eq. (2.9). The period of the first dynamic mode is 16.8 free-fall time units, which matches perfectly the period of the slow oscillation observed in the original dataset. The second dominant mode has a period of 1.6 free-fall time units, which fits the period of the fast plume emission determined from the original DNS data. The agreement between the sDMD results and the DNS data, and the distinct identification and separation of the two dominant spatio-temporal structures with frequencies that differ by an order of magnitude, gives further confidence in the capability of DMD to capture the relevant processes, be it in the temporal or spatial framework.

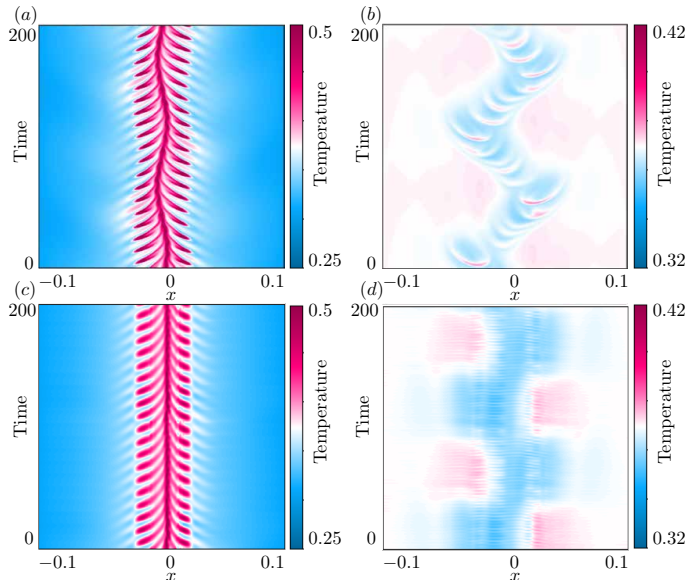


FIGURE 8. (a, b) Time evolution of the temperature of the original flow at a horizontal slice located at $y = H/2$ and at the height (a) $z = 0.1H$, to capture plume emission, and (b) $z = 0.8H$, to capture oscillations. (c, d) Time evolution of the temperature of the reconstructed field with the first 2 dominant modes. It is noted that the reconstruction (c) and (d) are based on different snapshot intervals.

3.3. Asymptotic Suction Boundary Layer (ASBL)

3.3.1. Fluid flows \mathcal{E} underlying dynamic equations

The ASBL is an open flow that develops over a flat bottom plate in the presence of suction through that plate. In consequence, the BL thickness remains constant in the streamwise direction, and the ASBL shares certain properties with parallel shear flows and spatially developing BLs. In the DNS, the ASBL is emulated by a plane Couette setup using a simulation domain with a large height. That is, we consider a fluid located in a wide gap between two parallel plates as shown schematically in fig. 9. The bottom plate is stationary and the fluid is set in motion through the top plate moving in the x -direction with velocity U_∞ . The latter corresponds to the free-stream velocity of the open flow. The flow is assumed to be incompressible and the conditions isothermal such that the density can be regarded as constant.

Expressed in units of the free-stream velocity, the laminar flow is given by

$$\mathbf{U} = \begin{pmatrix} 1 - e^{-yV_s/\nu} \\ -V_s/U_\infty \\ 0 \end{pmatrix}, \quad (3.5)$$

where V_s is the suction velocity and ν is the kinematic viscosity. The deviations \mathbf{u} of the laminar flow are then described by the dimensionless equations

$$\partial_t \mathbf{u} + \mathbf{u} \cdot \nabla \mathbf{u} + \mathbf{U} \nabla \mathbf{u} + \mathbf{u} \nabla \mathbf{U} + \nabla p - Re^{-1} \Delta \mathbf{u} = 0, \quad \nabla \cdot \mathbf{u} = 0, \quad (3.6)$$

where p is the pressure divided by the constant density ρ and $Re = U_\infty \delta / \nu$ the Reynolds number based on the free-stream velocity, the laminar displacement thickness $\delta = \nu / V_s$ and the kinematic viscosity of the fluid.

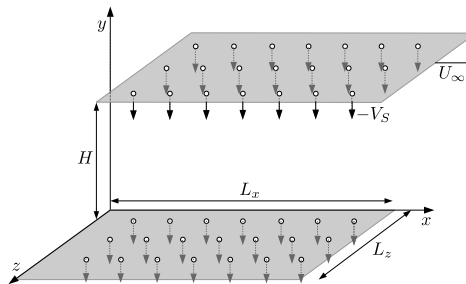


FIGURE 9. Schematic drawing of the asymptotic suction boundary layer in numerical simulations. The lower plate is stationary and the fluid is set in motion by the upper plate that moves in x -direction with velocity U_∞ , representing the free-stream velocity of the emulated open flow. Fluid is removed through a porous bottom plate with velocity V_S , to guarantee conservation of mass, fluid enters the system at the same speed through a porous top plate. In numerical simulations, this is realised uniformly through boundary conditions on the wall-normal component of the velocity field.

Re	Re_τ	$\tau_w/\rho U_\infty^2$	L_x/δ	H/δ	L_z/δ	N_x	N_y	N_z	$\Delta t/(\delta/U_\infty)$	N
1000	320	0.0003	4π	20	4.6π	64	161	96	1	4068

TABLE 1. Details of the ASBL simulations discussed in Sec. 3.3. The Reynolds number based on the free-stream velocity U_∞ and the laminar displacement thickness δ is denoted by Re . Re_τ is the friction Reynolds number, τ_w the shear stress at the bottom wall, ρ the density, U_∞ the free-stream velocity, L_x , H and L_z the length, height and width of the simulation domain, N_x , N_y and N_z the number of grid points in x , y and z -directions, respectively, Δt the sampling interval and N the number of samples.

3.3.2. Numerical details

The DNS data was generated with the open-source code `channelflow2.0` (Gibson 2014; Gibson *et al.* 2019). Equations (3.6) are solved numerically in a rectangular domain $\Omega = [-L_x/2, L_x/2] \times [0, H] \times [-L_z/2, L_z/2]$ as schematically shown in fig. 9, with periodic boundary conditions in the streamwise x - and the spanwise z -directions and no-slip boundary conditions in the wall-normal y -direction. `Channelflow2.0` uses the standard pseudospectral technique with $2/3^{\text{rd}}$ dealiasing in stream- and spanwise directions, where the spatial discretisation is by Fourier expansions in the homogeneous directions and a Chebychev expansion in the y -direction. The temporal discretisation is given by a third-order semi-implicit backward differentiation scheme (SBDF3). Details of the DNS dataset are summarised in table I. The occurrence of large-scale persistent coherent flow structures of long streamwise extent is one of the striking features in turbulent BLs, and ASBL is no exception.

3.3.3. Streaming DMD

We attempt to describe the dynamics of such a large-scale structure in a long time series using a small number of dynamic modes. In order to alleviate the computational effort, the simulations were carried out at moderate Reynolds number using a short computational domain in the streamwise direction and the sampled flow fields were averaged in streamwise direction. As such, the analysed two-dimensional fields obtained by streamwise

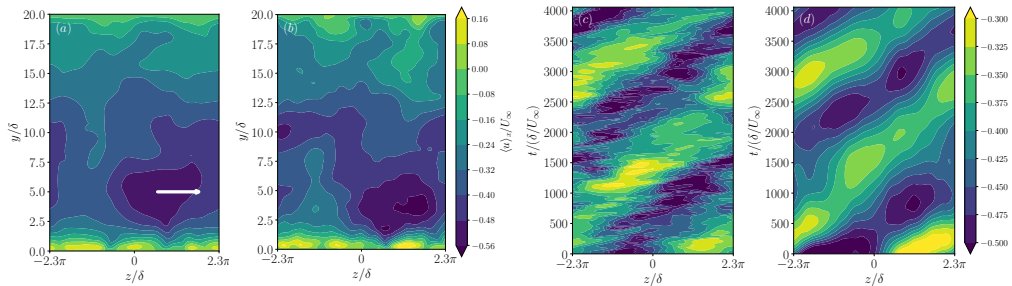


FIGURE 10. Spatio-temporal structure and reconstruction of large-scale dynamics in the asymptotic suction boundary layer. (a) Representative original velocity-field sample. The colour coding indicated the streamwise-averaged deviation $\langle u \rangle_x$ from laminar flow in streamwise direction. A slow large-scale coherent structure is clearly visible, its horizontal movement is indicated by the white arrow. (b) Reconstructed flow field using the first two dynamic modes. (c) Time evolution of the original flow at the centre of the coherent structure at $y/\delta \simeq 6$. (d) Time evolution of the reconstructed flow from the first two dynamic modes at $y/\delta \simeq 6$.

averaging adequately represent the three-dimensional fields at least concerning the large-scale dynamics with streamwise coherence that is of interest here. Figure 10(a) shows the deviations from the laminar flow averaged in the streamwise direction of a typical sample. A large-scale coherent region that is localised in the spanwise direction and extends from about 2δ to 7δ in wall-normal direction is clearly visible. This structure moves slower than the laminar flow and is accompanied by near-wall small-scale regions where the flow is faster than the laminar flow. The slow large-scale structure drifts through the simulation domain in spanwise direction as indicated by the white arrow in figure 10(a). The spanwise shift occurs with velocity $c = (L_z/\delta)/(2000\delta/U_\infty) \approx 0.007U_\infty$ as evidenced by the periodic pattern in the spatio-temporal evolution of the flow at a fixed distance $y/\delta = 6$ from the bottom plate shown in figure 10(c). That is, it takes the large-scale coherent structure approximately 2000 time units to cross the simulation domain once. During that time it varies in intensity, as can be seen when considering the diagonal pattern shown in the spatio-temporal evolution presented in fig. 10(c), it does not seem to disappear completely and it is difficult to discern a pattern in the evolution.

The aim is to reconstruct the dominant spatio-temporal scales of the dynamics, i.e. the spatial extent of the slow large-scale structure and the slow spanwise drift, with a few dynamic modes. To capture the latter requires a very long time series and as such the application of streaming DMD as opposed to classical DMD, as not all data can be stored in memory at the same time. As can be seen by comparison of the reconstructed data in shown in fig. 10(b) with the original data shown in fig. 10(a), the wall-normal and spanwise extent of the large-scale coherent structure and the small-scale fast flow regions are well reproduced by only the first two dynamic modes. Similarly, two dynamic modes suffice to reproduce the slow spanwise drift with velocity c as demonstrated by comparison of the spatio-temporal evolution of the reconstructed flow shown in fig. 10(d) with that of the original data shown in figure 10(c). The distinctive maxima and minima that are present in the diagonal pattern of the reconstructed flow evolution in fig. 10(d) reveal the presence of slow periodicity in the structure's intensity, which is not clearly visible in the full dynamics.

4. Conclusion & Outlooks

In this paper we demonstrated the applicability of streaming DMD (Hemati *et al.* 2014), an efficient low-storage version of the classical SVD-based DMD (Schmid 2010), for the analysis of turbulent flows that show a certain degree of spatio-temporal coherence. We first validate the proposed streaming DMD by comparing it to the classical SVD-based DMD (Schmid 2010), based on the example of the flow past a cylinder for $Re = 100$. The comparison shows that the obtained streaming dynamic modes and eigenvalues match well with those computed from a post-processing implementation of the SVD-based DMD given enough truncation modes. However, streaming DMD can handle considerably larger datasets with less computational costs compared to the SVD-based DMD, thanks to the feature of incremental data updating, which only requires two data samples to be held in memory at a given time.

The objective of this study was to extract the main dynamic features with an efficient data-driven method and use the resulting information for a low-dimensional reconstruction of the flow. We considered three examples, namely rapidly rotating turbulent Rayleigh–Bénard convection, horizontal convection, and asymptotic suction BL. For rapidly rotating turbulent RBC, a dominant zonal flow pattern, the boundary zonal flow, was identified through the first two dynamic modes. Similarly, for horizontal convection two processes that operate on different time scales could be clearly classified in terms of dynamic modes: The second dynamic mode captures the slow oscillatory dynamics in the bulk while the third dynamic mode describes the much faster process of thermal plume emission. Finally, for ASBL a distinctive coherent low-momentum zone that travels through the simulation domain in spanwise direction can be well described by the only first two dynamic modes. These examples show that the incrementally updated DMD algorithm can successfully decompose the dominant structures with corresponding frequencies and modes. This establishes sDMD as an accurate and efficient method to identify and capture dominant spatio-temporal features from large datasets of highly-turbulent flows.

As DMD decomposes datasets into coherent structures based on characteristic frequencies, it is especially useful for the analysis of flows featuring large-scale coherent structures and periodic motion. The advantages of the sDMD algorithm, both in terms of low-storage and potential real-time implementation, will make DMD available in numerous contexts where it would have been infeasible previously. This includes in particular the analysis of massive datasets that cannot completely reside in memory. One such application, for instance, concerns the search for unstable periodic orbits in turbulent flows, where a classical DMD-based approach has been successfully applied at moderate Reynolds number (Page & Kerswell 2020). Streaming DMD may constitute a step forward in extending the applicability of this method to higher Reynolds numbers.

In the further steps, the streaming DMD can be applied to different turbulent flow datasets, to investigate in detail the ability to decompose coherent flow structures. One disadvantage of streaming DMD is that the truncation number of snapshots to achieve the similar reconstruction accuracy as the SVD-based DMD is typically larger. Here we have not considered the effect of the truncation number but have only focused on the analysis of the first several dominant modes. The truncation number is, however, important and should be quantitatively considered when applying the streaming DMD to flow field reconstruction or decomposition of complex turbulent flows with multi-frequency temporal structures.

Finally we want to mention that not only DMD but also some other approaches, based on or related to DMD, might be very efficient in extraction and analysis of the dynamics

of the turbulent superstructures. While in the DMD we apply linear transformations to obtain modes out of snapshots and vice versa, a natural extension of the DMD would be to employ non-linear transformations instead. This can be realized either via application of hand-picked nonlinear functions (e.g. to use so-called extending DMD – eDMD, see Williams *et al.* (2015)), or by training a deep neural network (e.g. to use deep Koopman models like Morton *et al.* (2018)). A multilayer convolutional neural network appears to be a good candidate for such a task. In general, (un)supervised deep learning seems to be very promising in the problems of the extraction and analysis of the global dynamics of the turbulent flow superstructures. A more detailed consideration of these alternate approaches is beyond the scope of this article and application of these advanced methods for the turbulent superstructure analysis remains a challenge for future studies.

Acknowledgments

This work is supported by the Max Planck Center for Complex Fluid Dynamics, the Priority Programme SPP 1881 "Turbulent Superstructures" of the Deutsche Forschungsgemeinschaft (DFG) under grants Sh405/7 and Li3694/1 and DFG grants Sh405/8 and Sh405/10. The authors acknowledge the Leibniz Supercomputing Centre (LRZ) and the Lichtenberg high performance computer of the TU Darmstadt for providing computing time.

REFERENCES

- AHLERS, G., GROSSMANN, S. & LOHSE, D. 2009 Heat transfer and large scale dynamics in turbulent Rayleigh–Bénard convection. *Rev. Mod. Phys.* **81** (2), 503.
- ANANTHARAMU, S. & MAHESH, K. 2019 A parallel and streaming dynamic mode decomposition algorithm with finite precision error analysis for large data. *J. Comput. Phys.* **380**, 355–377.
- BAGHERI, S. 2013 Koopman-mode decomposition of the cylinder wake. *J. Fluid Mech.* **726**, 596–623.
- BAILON-CUBA, J., SHISHKINA, O., WAGNER, C. & SCHUMACHER, J. 2012 Low-dimensional model of turbulent mixed convection in a complex domain. *Phys. Fluids* **24** (10), 107101.
- BERKOOZ, G., HOLMES, P. & LUMLEY, J. L. 1993 The proper orthogonal decomposition in the analysis of turbulent flows. *Annu. Rev. Fluid Mech.* **25** (1), 539–575.
- BRUNTON, B. W., JOHNSON, L. A., OJEMANN, J. G. & KUTZ, J. N. 2016 Extracting spatial-temporal coherent patterns in large-scale neural recordings using dynamic mode decomposition. *J. Neurosci. Methods* **258**, 1–15.
- BRUNTON, S. L. & NOACK, B. R. 2015 Closed-loop turbulence control: progress and challenges. *Appl. Mech. Rev* **67** (5).
- FAVIER, B. & KNOBLOCH, E. 2020 Robust wall modes in rapidly rotating Rayleigh–Bénard convection. *J. Fluid. Mech.* **895**, R1.
- FAZLE HUSSAIN, A. K. 1986 Coherent structures and turbulence. *J. Fluid Mech.* **173**, 303–356.
- GAVISH, M. & DONOHO, D. L. 2014 The optimal hard threshold for singular values is $4/\sqrt{3}$. *IEEE. T. Inform. Theory* **60**, 5040–5053.
- GHOOREYSHI, M., JIRASEK, A. & CUMMINGS, R. M. 2014 Reduced order unsteady aerodynamic modeling for stability and control analysis using computational fluid dynamics. *Prog. Aerosp. Sci* **71**, 167–217.
- GIBSON, J. F. 2014 Channelflow: A spectral Navier–Stokes simulator in C++. *Tech. Rep.*. U. New Hampshire.
- GIBSON, J. F., REETZ, F., AZIMI, S., FERRARO, A., KREILOS, T., SCHROBSDORFF, H., FARANO, M., YESIL, A. F., SCHÜTZ, S. S., CULPO, M. & SCHNEIDER, T. M. 2019 Channelflow 2.0. <https://www.channelflow.ch>.
- GRAMBERG, H., HOWELL, P. & OCKENDON, J. 2007 Convection by a horizontal thermal gradient. *J. Fluid Mech.* **586**, 41–57.

- GROSSMANN, S., LOHSE, D. & SUN, C. 2016 High-Reynolds number Taylor–Couette turbulence. *Annu. Rev. Fluid Mech.* **48**, 53–80.
- HEMATI, M. S., WILLIAMS, M. O. & ROWLEY, C. W. 2014 Dynamic mode decomposition for large and streaming datasets. *Phys. Fluids* **26** (11), 111701.
- HOLMES, P., LUMLEY, J. L. & BERKOOZ, G. 1996 *Turbulence, Coherent Structures, Dynamical Systems and Symmetry*. Cambridge University Press.
- HORN, S. & SCHMID, P. J. 2017 Prograde, retrograde, and oscillatory modes in rotating Rayleigh–Bénard convection. *J. Fluid Mech.* **831**, 182–211.
- HUGHES, G. O. & GRIFFITHS, R. W. 2008 Horizontal Convection. *Annu. Rev. Fluid Mech.* **40** (1), 185–208.
- HUTCHINS, N. & MARUSIC, I. 2007 Evidence of very long meandering structures in the logarithmic region of turbulent boundary layers. *J. Fluid Mech.* **579**, 1–28.
- HUTCHINS, N. & MARUSIC, I. 2011 High Reynolds number wall turbulence. *Annu. Rev. Fluid Mech.* **43**, 353–375.
- JONES, C. W. & WATSON, E. J. 1963 Two-dimensional boundary layers. In *Laminar Boundary Layers* (ed. L. Rosenhead). Oxford University Press.
- JOVANOVIĆ, M. R., SCHMID, P. J. & NICHOLS, J. W. 2014 Sparsity-promoting dynamic mode decomposition. *Phys. Fluids* **26** (2), 024103.
- KATUL, G. G. 2019 The anatomy of large-scale motion in atmospheric boundary layers. *J. Fluid Mech.* **858**, 1–4.
- KOOLJ, G. L., BOTCHEV, M. A., FREDERIX, E. M., GEURTS, B. J., HORN, S., LOHSE, D., VAN DER POEL, E. P., SHISHKINA, O., STEVENS, R. J. & VERZICCO, R. 2018 Comparison of computational codes for direct numerical simulations of turbulent Rayleigh–Bénard convection. *Comput. Fluids* **166**, 1–8.
- KOOPMAN, B. O. 1931 Spectrum of the Koopman operator, spectral expansions in functional spaces, and state-space geometry. *Proc. N. Acad. Sci.* **17**, 315–318.
- KOU, J. & ZHANG, W. 2017 An improved criterion to select dominant modes from dynamic mode decomposition. *Eur. J. Mech. B Fluids* **62**, 109–129.
- KUTZ, J. N., BRUNTON, S. L., BRUNTON, B. W. & PROCTOR, J. L. 2016 *Dynamic mode decomposition: data-driven modeling of complex systems*. SIAM.
- LOHSE, D. & XIA, K. Q. 2010 Small-scale properties of turbulent Rayleigh–Bénard convection. *Annu. Rev. Fluid Mech.* **42** (1), 335–364.
- MARUSIC, I., MATHIS, R. & HUTCHINS, N. 2010 Predictive model for wall-bounded turbulent flow. *Science* **329**, 193–196.
- MEINHART, C. D. & ADRIAN, R. J. 1995 On the existence of uniform momentum zones in a turbulent boundary layer. *Phys. Fluids* **7**, 694–696.
- MEZIĆ, I. 2005 Spectral properties of dynamical systems, model reduction and decompositions. *Nonlinear Dyn.* **41**, 309–325.
- MEZIĆ, I. 2019 Spectrum of the Koopman operator, spectral expansions in functional spaces, and state-space geometry. *J. Nonlinear Sci.* pp. 1–55.
- MONTY, J. P., STEWART, J. A., WILLIAMS, R. C. & CHONG, M. S. 2007 Large-scale features in turbulent pipe and channel flows. *J. Fluid Mech.* **589**, 147–156.
- MORTON, J., WITHERDEN, F. D., JAMESON, A. & KOCHENDERFER, M. J. 2018 Deep Dynamical Modeling and Control of Unsteady Fluid Flows. In *NeurIPS*.
- PAGE, J. & KERSWELL, R. R. 2020 Searching turbulence for periodic orbits with dynamic mode decomposition. *J. Fluid Mech.* **886**, A28.
- PODVIN, B. & LUMLEY, J. 1998 A low-dimensional approach for the minimal flow unit. *J. Fluid Mech.* **362**, 121–155.
- PROCTOR, J. L., BRUNTON, S. L. & KUTZ, J. N. 2016 Dynamic mode decomposition with control. *SIAM J. Appl. Dyn. Syst.* **15** (1), 142–161.
- REITER, P. & SHISHKINA, O. 2020 Classical and symmetrical horizontal convection: detaching plumes and oscillations. *J. Fluid Mech.* **892**, R1.
- ROWLEY, C. W., COLONIUS, T. & MURRAY, R. M. 2004 Model reduction for compressible flows using POD and Galerkin projection. *Physica D* **189**, 115–129.
- ROWLEY, C. W. & DAWSON, S. T. 2017 Model reduction for flow analysis and control. *Annu. Rev. Fluid Mech.* **49**, 387–417.

- ROWLEY, C. W., MEZIĆ, I., BAGHERI, S., SCHLATTER, P. & HENNINGSON, D. S. 2009 Spectral analysis of nonlinear flows. *J. Fluid Mech.* **641**, 115–127.
- SCHLICHTING, H. 1979 *Boundary Layer Theory*. McGraw-Hill.
- SCHMID, P. J. 2010 Dynamic mode decomposition of numerical and experimental data. *J. Fluid Mech.* **656**, 5–28.
- SCOTT, J. R., MAROTZKE, J. & ADCROFT, A. 2001 Geothermal heating and its influence on the meridional overturning circulation. *J. Geophys. Res.* **106** (C12), 31141–31154.
- SHISHKINA, O. 2020 Tenacious wall states in thermal convection in rapidly rotating containers. *J. Fluid. Mech.* **898**, F1.
- SHISHKINA, O., GROSSMANN, S. & LOHSE, D. 2016 Heat and momentum transport scalings in horizontal convection. *Geophys. Res. Lett.* **43** (3), 1219–1225.
- SHISHKINA, O., HORN, S., WAGNER, S. & CHING, E. S. 2015 Thermal boundary layer equation for turbulent Rayleigh–Bénard convection. *Phys. Rev. Lett.* **114** (11), 114302.
- SHISHKINA, O., STEVENS, R. J. A. M., GROSSMANN, S. & LOHSE, D. 2010 Boundary layer structure in turbulent thermal convection and its consequences for the required numerical resolution. *New J. Phys.* **12** (7), 75022.
- SIGGIA, E. D. 1994 High Rayleigh number convection. *Annu. Rev. Fluid Mech.* **26** (1), 137–168.
- SPIEGEL, E. A. 1971 Convection in stars I. Basic Boussinesq convection. *Annu. Rev. Astron. Astrophys.* **9** (1), 323–352.
- TISSOT, G., CORDIER, L., BENARD, N. & NOACK, B. R. 2014 Model reduction using dynamic mode decomposition. *CR. Mecanique* **342** (6-7), 410–416.
- WILLIAMS, M. O., KEVREKIDIS, I. G. & ROWLEY, C. W. 2015 A data-driven approximation of the Koopman operator: extending dynamic mode decomposition. *J. Nonlinear Sci.* **25**, 1307–1346.
- YAGLOM, A. & TATARSKI, V. 1967 The structure of inhomogeneous turbulence. In *Atmospheric Turbulence and Radio Wave Propagation*, pp. 166–178. Nauka.
- ZHANG, H., ROWLEY, C. W., DEEM, E. A. & CATTAFESTA, L. N. 2019 Online dynamic mode decomposition for time-varying systems. *SIAM J. Appl. Dyn. Syst.* **18** (3), 1586–1609.
- ZHANG, X., VAN GILS, D. P., HORN, S., WEDI, M., ZWIRNER, L., AHLERS, G., ECKE, R. E., WEISS, S., BODENSCHATZ, E. & SHISHKINA, O. 2020 Boundary zonal flow in rotating turbulent Rayleigh–Bénard convection. *Phys. Rev. Lett.* **124** (8), 084505.